Electronic Supplementary Material (ESI) for Journal of Materials Chemistry A.

Supplementary Information for the Effect of pore size on the process of CO_2 adsorption in MIL-101, MOF-177, and UiO-66

Gunjan Auti,[†] Yuki Kametani,[‡] Hibiki Kimura,[†] Soumyadeep Paul,[†] Wei-Lun Hsu,[†] Shinpei Kusaka,[¶] Rytaro Matsuda,[¶] Takashi Uemura,[‡] Shohei Chiashi,[†] and Hirofumi Daiguji*[,†]

†*Department of Mechanical Engineering, The University of Tokyo, 7-3-1 Hongo, Bunkyo-ku, Tokyo 113-8656, Japan*

‡*Department of Applied Chemistry, The University of Tokyo, 7-3-1 Hongo, Bunkyo-ku, Tokyo 113-8656, Japan*

¶*Department of Materials Chemistry, Nagoya University,Furo-cho, Chikusa-ku, Nagoya 464-8603, Japan*

E-mail: daiguji@thml.t.u-tokyo.ac.jp

S1 MOF Characterization

S1.1 X-Ray Diffraction Images

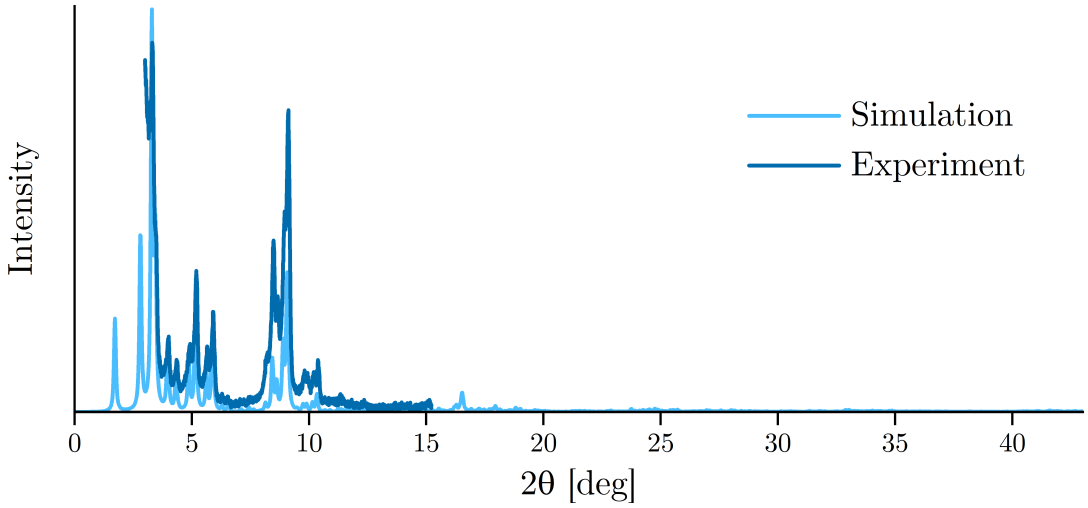

Figure S1: X-Ray diffraction data for the MIL-101 sample.

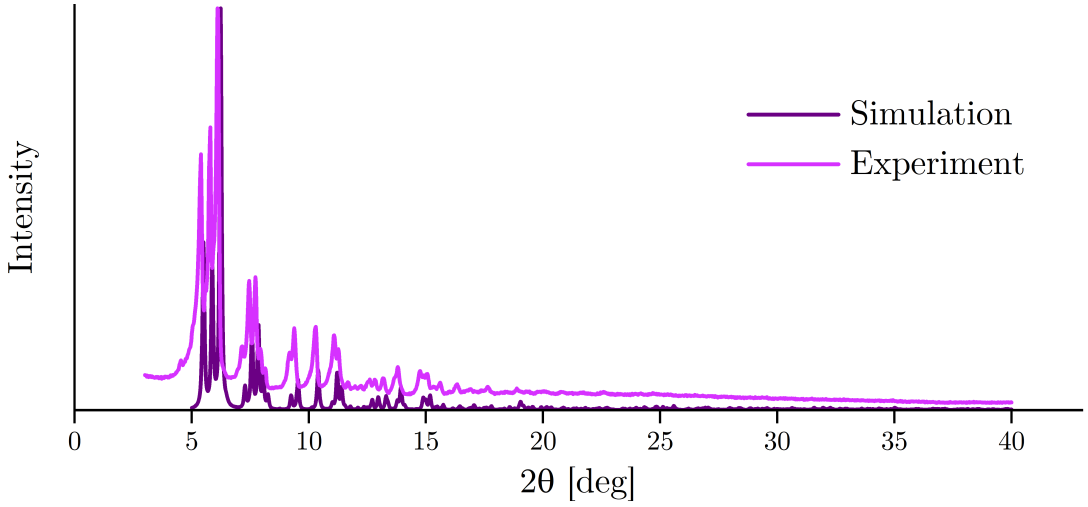

Figure S2: X-Ray diffraction data for the MOF-177 sample.

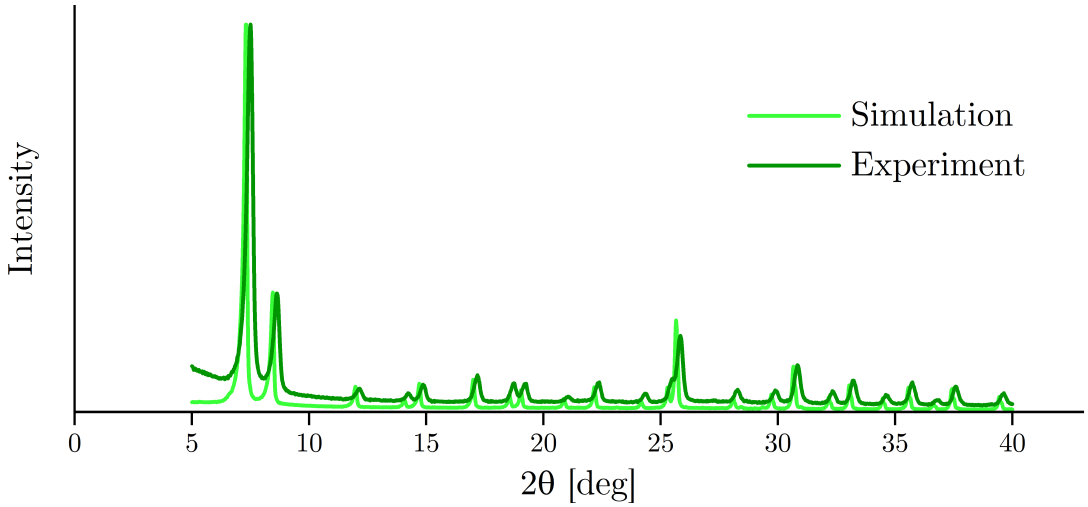

Figure S3: X-Ray diffraction data for the UiO-66 sample.

S1.2 Nitrogen Adsorption Isotherm

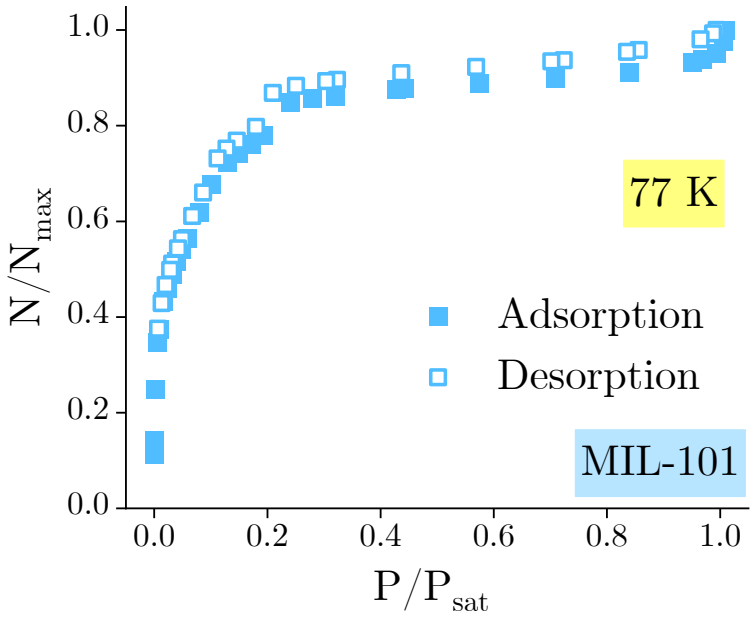

Figure S4: Nitrogen adsorption-desorption isotherm at 77 K for MIL-101.

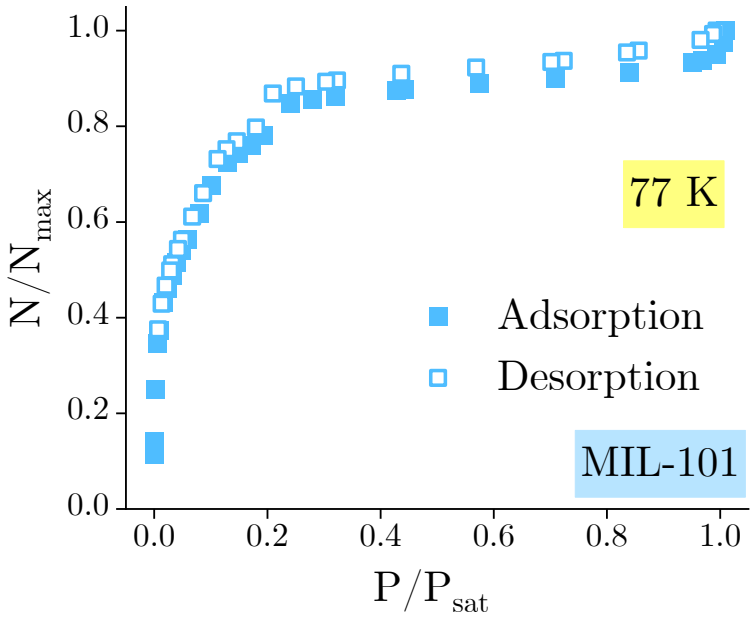

Figure S5: Nitrogen adsorption-desorption isotherm at 77 K for MOF-177.

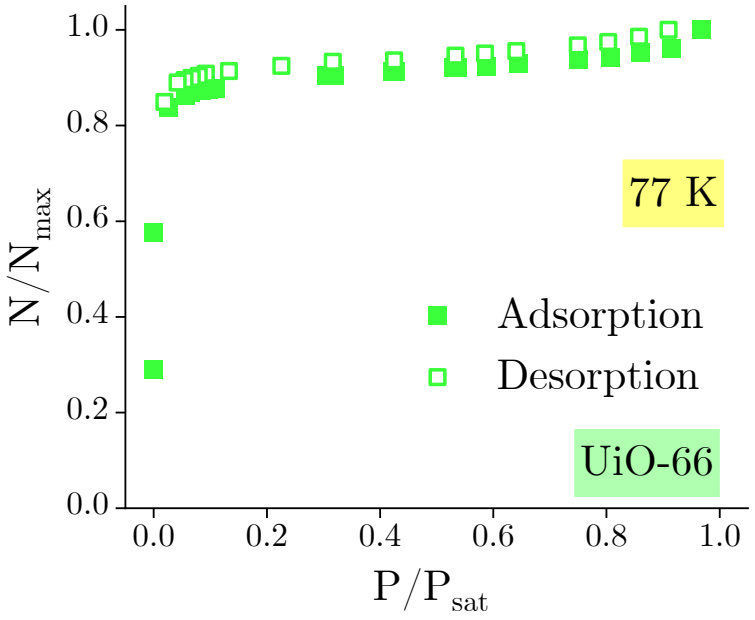

Figure S6: Nitrogen adsorption-desorption isotherm at 77 K for UiO-66.

S2 Enthalpy of Adsorption

Heat flow curves were obtained from the Calvet-type calorimeter (Microcalvet Ultra, Setaram) for the adsorption and desorption processes. The enthalpy of adsorption is calculated by integrating the heat flow curves for each pressure step.

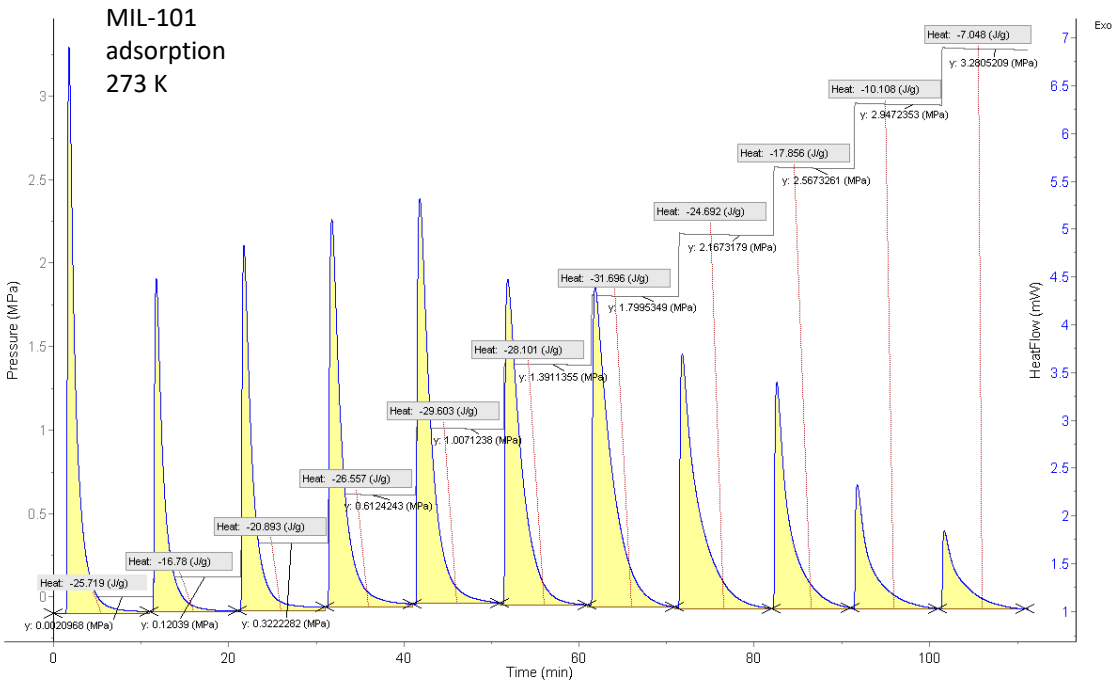

Figure S7: MIL-101 heat flow curve at 273 K during the adsorption process.

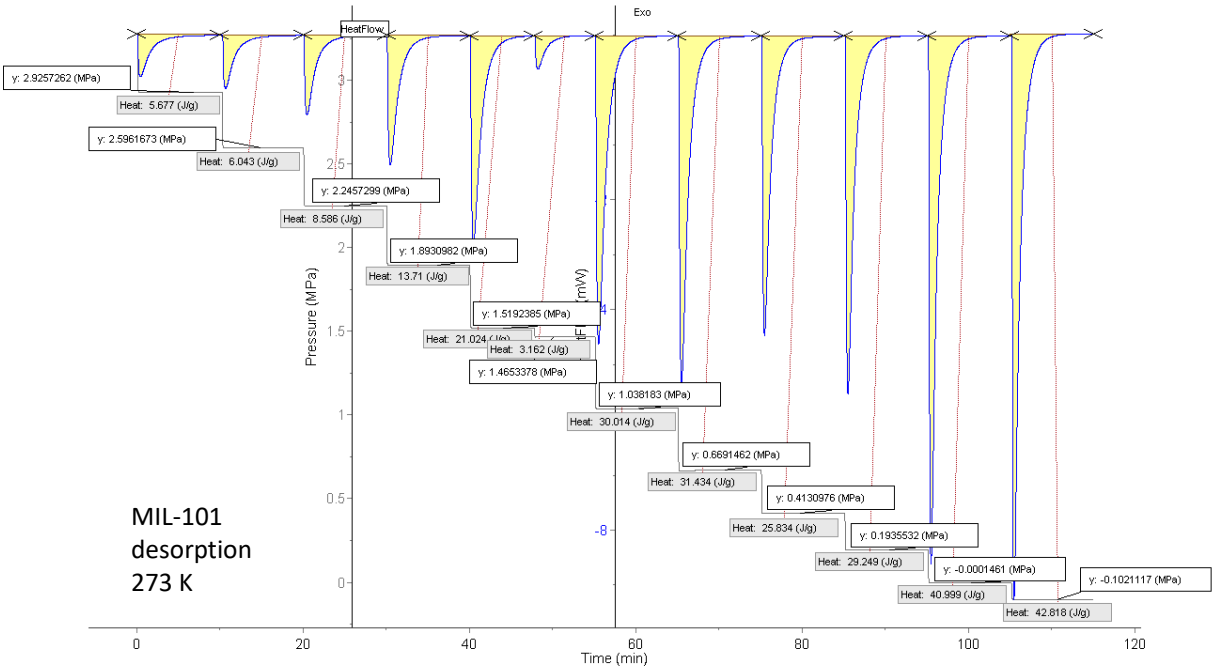

Figure S8: MIL-101 heat flow curve at 273 K during the desorption process.

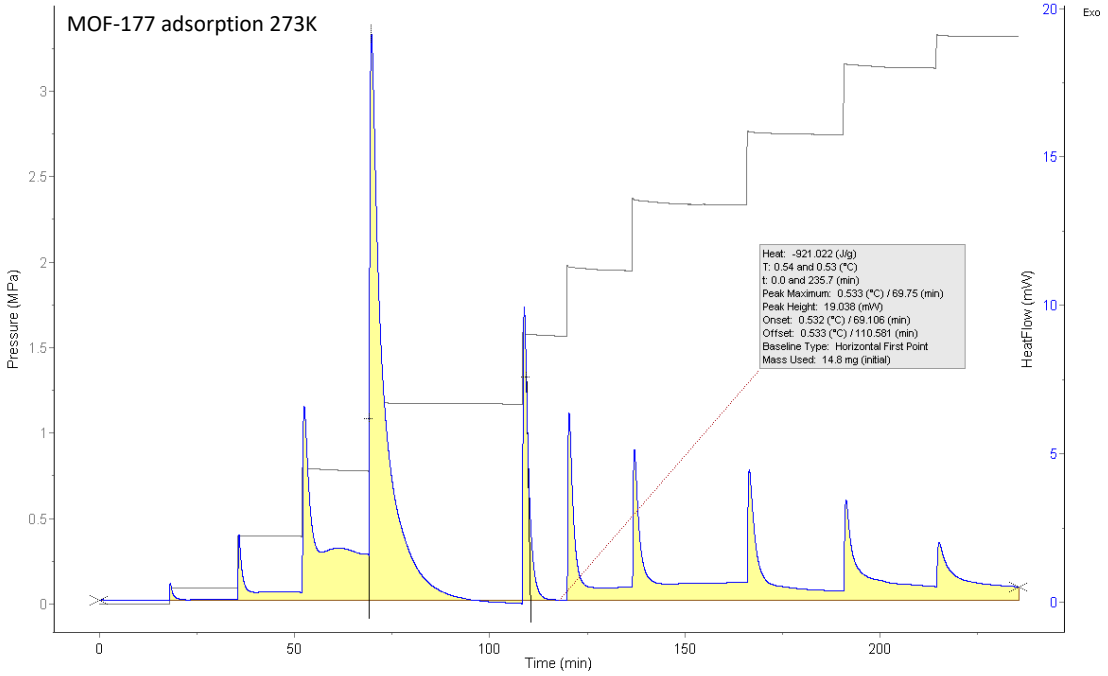

Figure S9: MOF-177 heat flow curve at 273 K during the adsorption process.

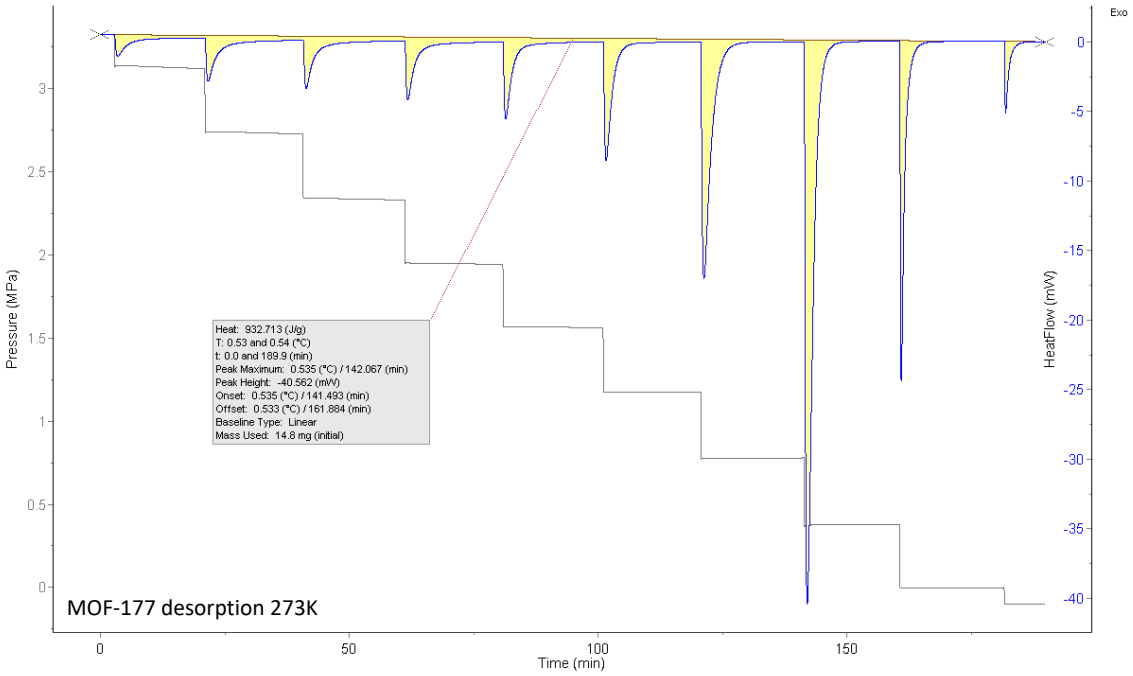

Figure S10: MOF-177 heat flow curve at 273 K during the desorption process.

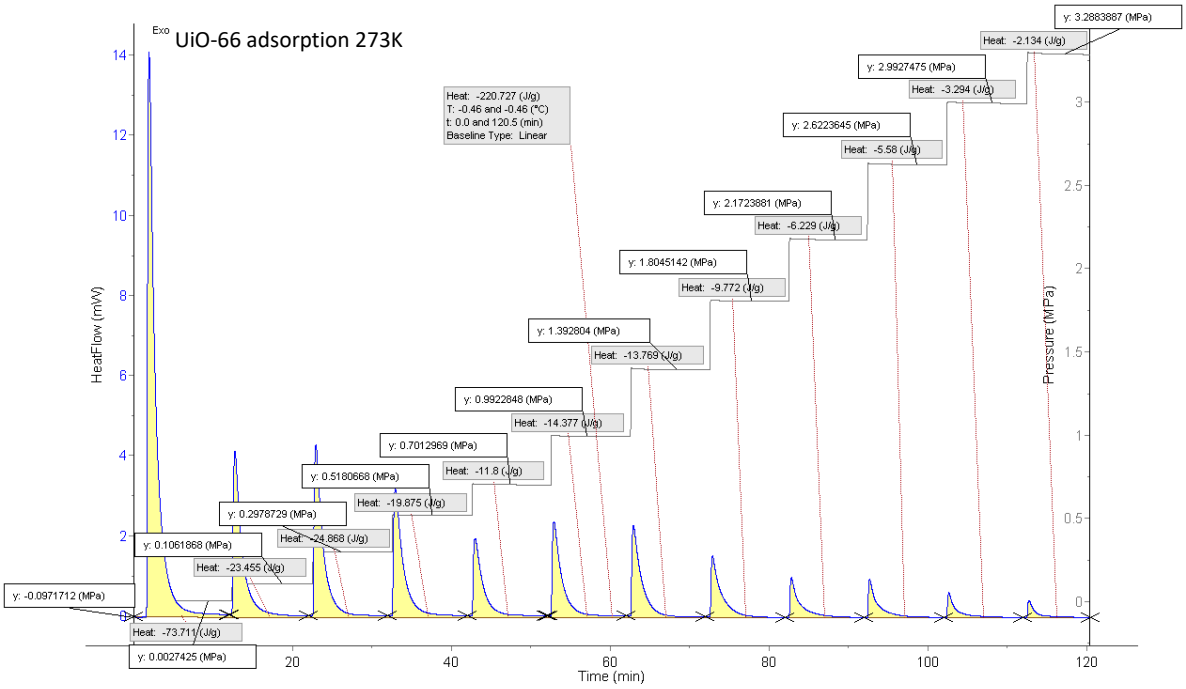

Figure S11: UiO-66 heat flow curve at 273 K during the adsorption process.

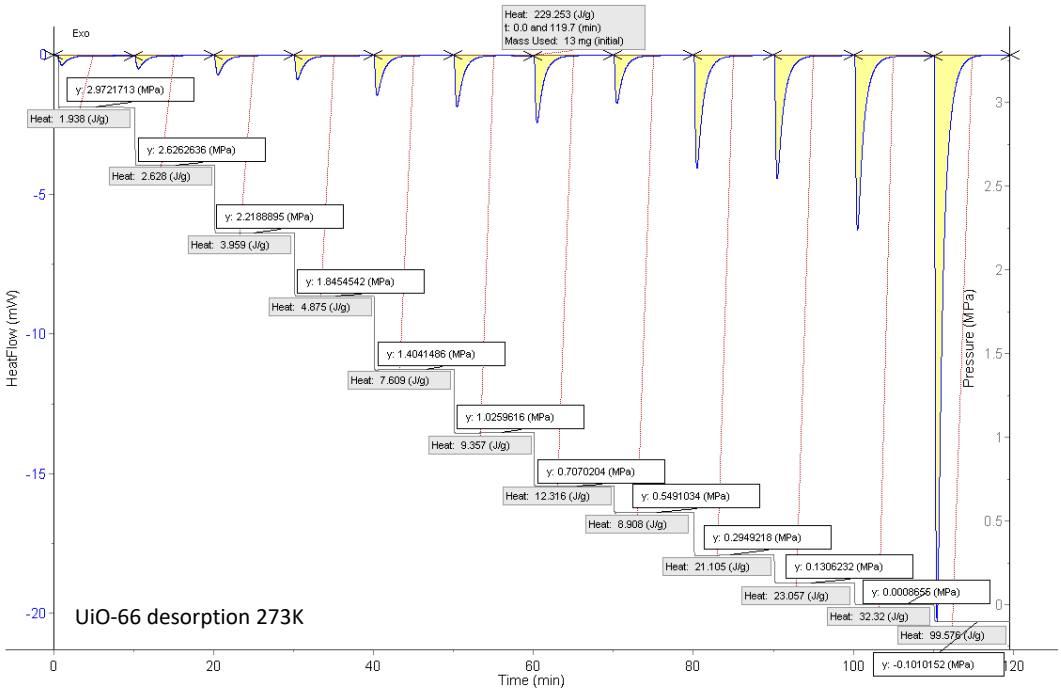

Figure S12: UiO-66 heat flow curve at 273 K during the desorption process.

S3 Grand Canonical Monte Carlo Simulation

The Lennard–Jones parameters and the grand canonical Monte Carlo (GCMC) formulation used in the simulation are given in this section.[1]

S3.1 GCMC Scheme

$$U_{\mathrm{VDW}} = 4\epsilon_{ij}\left[\left(\frac{\sigma_{ij}}{r_{ij}}\right)^{12} - \left(\frac{\sigma_{ij}}{r_{ij}}\right)^{6}\right] \tag{1}$$

The mixing potential parameters are calculated using the Lorentz–Berthelot rules:

$$\epsilon_{ij} = \sqrt{\epsilon_i \epsilon_j}; \quad \sigma_{ij} = \frac{1}{2}(\sigma_i + \sigma_j) \tag{2}$$

The Coulombic interactions between charged particles are modeled using the Ewald method:

$$U_{\mathrm{c}} = U^{\mathrm{real}} + U^{\mathrm{rec}} \tag{3}$$

where the two components of the Coulombic potential $\mathrm{U}^{\mathrm{real}}$ and $\mathrm{U}^{\mathrm{rec}}$ are expressed as:

$$U^{\mathrm{real}} = \sum_{i<j} q_i q_j \frac{\mathrm{erfc}(\alpha r_{ij})}{r_{ij}} \tag{4}$$

$$U^{\mathrm{rec}} = \frac{2\pi}{V}\sum_{\mathbf{k}\neq 0}\frac{1}{k^2}e^{-\frac{k^2}{4\alpha^2}}\left(\left|\sum_{i=1}^{N} q_i \cos\left(\mathbf{k}\cdot\mathbf{r}_i\right)\right|^2 + \left|\sum_{i=1}^{N} q_i \sin\left(\mathbf{k}\cdot\mathbf{r}_i\right)\right|^2\right) - \sum_i \frac{\alpha}{\sqrt{\pi}} q_i^2 \tag{5}$$

S3.2 L–J Parameters and CO_2 Model

Table T1: Lennard–Jones parameters for the MOFs[1]

MOF	Element	L–J Parameters	
		ϵ [K]	σ [Å]
UiO-66	Zr	34.7221	2.7832
	O	48.1581	3.0332
	C	47.8562	3.4730
	H	7.6489	2.8464
MOF-177	Zn	62.3992	2.4616
	O	48.1581	3.0332
	C	47.8562	3.4730
	H	7.6489	2.8464
MIL-101	Cr	7.5483	2.6932
	O	48.1581	3.0332
	C	47.8562	3.4730
	F	36.4834	3.0932
	H	7.6489	2.8464

Table T2: TraPPE model parameters for CO_2[2]

Atom	Type	ε [K]	σ [Å]	q [e]
C	O=[C]=O	27.0	2.80	0.70
O	[O]=C=O	79.0	3.05	-0.35
O	O=C=[O]	79.0	3.05	-0.35

Table T3: Bond lengths for CO_2 according to TraPPE model[2]

Stretch	Type	Length [Å]
1–2	(O=C)=O	1.16
2–3	O=(C=O)	1.16

Table T4: Bond angles for CO_2 according to TraPPE model[2]

Bend	**Type**	θ [deg]
2–1–3	O=C=O	180

S3.3 Simulation and Experimental Results

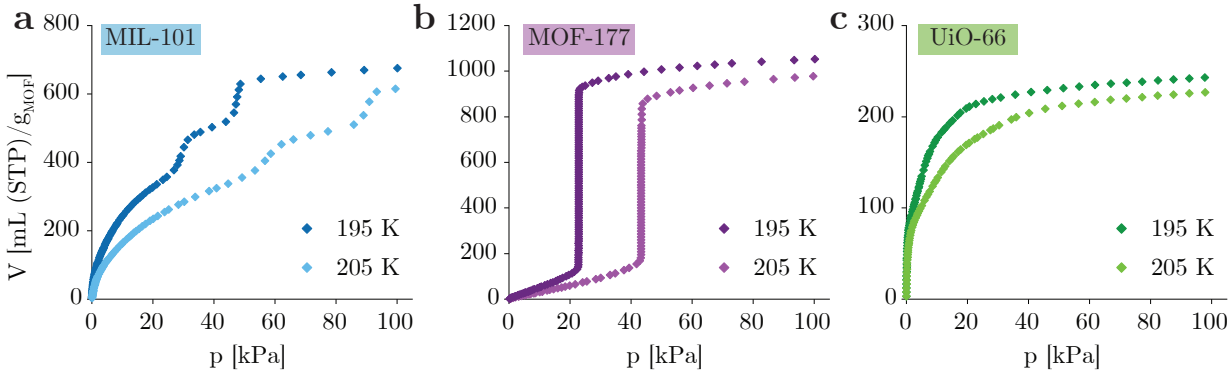

Figure S13: Experimental adsorption isotherms at 195 K and 205 K.

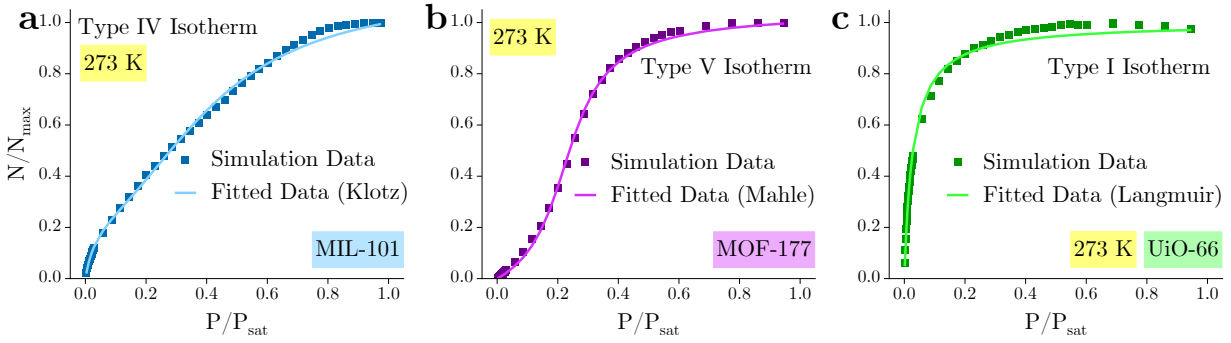

Figure S14: Adsorption isotherm obtained from the GCMC simulations at 273 K. The fitting parameters for each isotherm are listed in a later section.

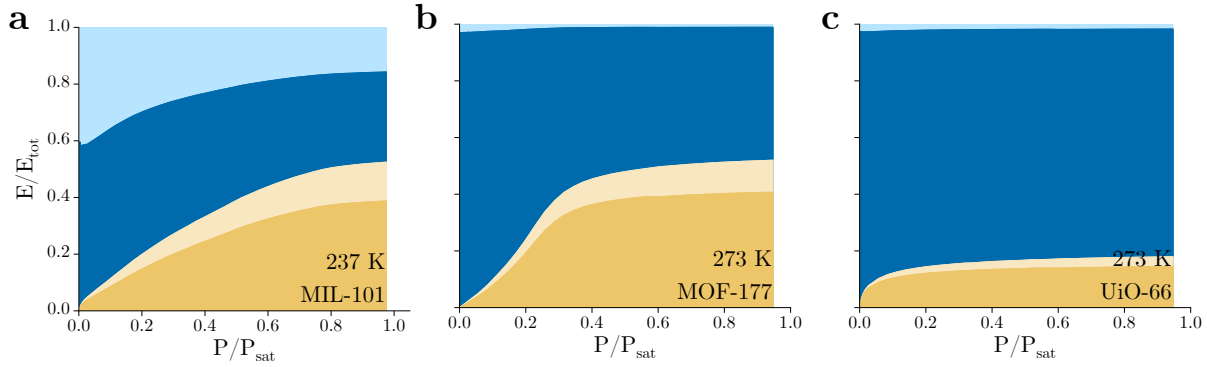

Figure S15: Interaction energy budget obtained from the GCMC simulations at 273 K.

S3.4 Pore-filling Process

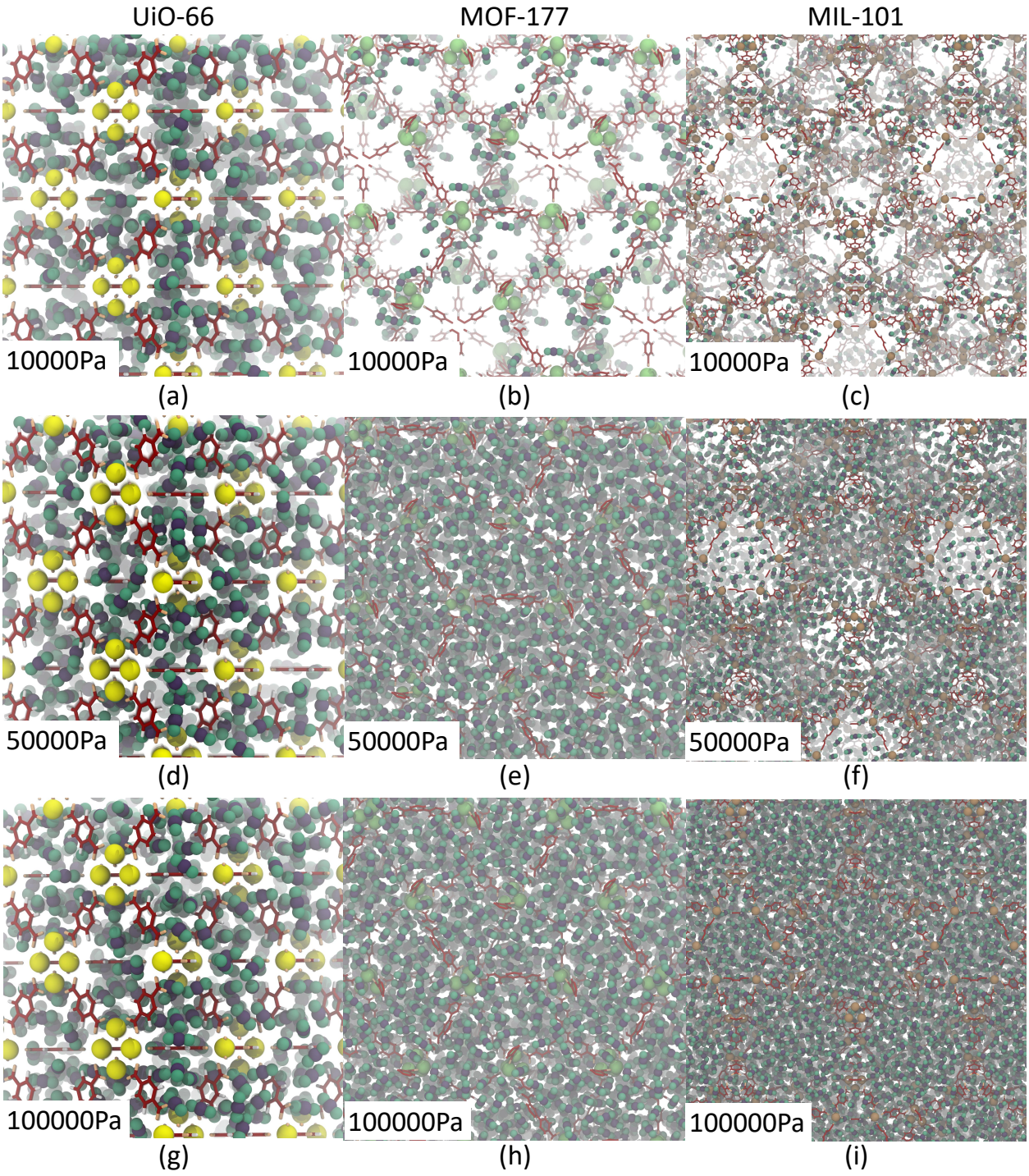

Figure S16: Pore-filling process.

S3.5 Isotherm Fitting

The type IV isotherms are modeled using Klotz theory,[3,4] as given by

$$\frac{N}{N_{max}} = \frac{Cq(1-(1+m)q^m+mq^{m+1})}{(1-q)(1+(C-1)q-Cq^{m+1})} \tag{6}$$

where,

$$q = \frac{Kp}{p_{sat}} = KP^* \tag{7}$$

The m, C, and K are the fitting parameters valued at 4.8192 ± 0.16159, 13.0442 ± 1.61476, and 2.3236 ± 0.05718, respectively, with an R-square value of 0.99787.

The isotherm is modeled using a form given by Mahle[5] as

$$\frac{N}{N^{max}} = \frac{1}{D}(tan^{-1}(\frac{P^*-A}{B}) - tan^{-1}(\frac{-A}{B})) \tag{8}$$

where D is,

$$D = tan^{-1}(\frac{1-A}{B}) - tan^{-1}(\frac{-A}{B}) \tag{9}$$

The fitting parameters in Eq. 8 are A = 0.22275 ± 0.00199 and B = -0.10738 ± 0.00294 with an R-square value of 0.99904. The Type I adsorption mechanism can be modeled using single-site Langmuir theory as

$$\frac{N}{N^{max}} = \frac{bP^*}{1+bP^*} \tag{10}$$

The fitting parameter is b = 35.24596 ± 0.84979, with an R-square value of 0.99382.

S4 UiO-n Family

As discussed in the main manuscript, to eliminate the effect of coulombic interaction we perform a similar analysis on the MOFs UiO-66, UiO-67, and UiO-68. The obtained results are plotted in this section. The adsorption isotherms change from Type I to Type V as

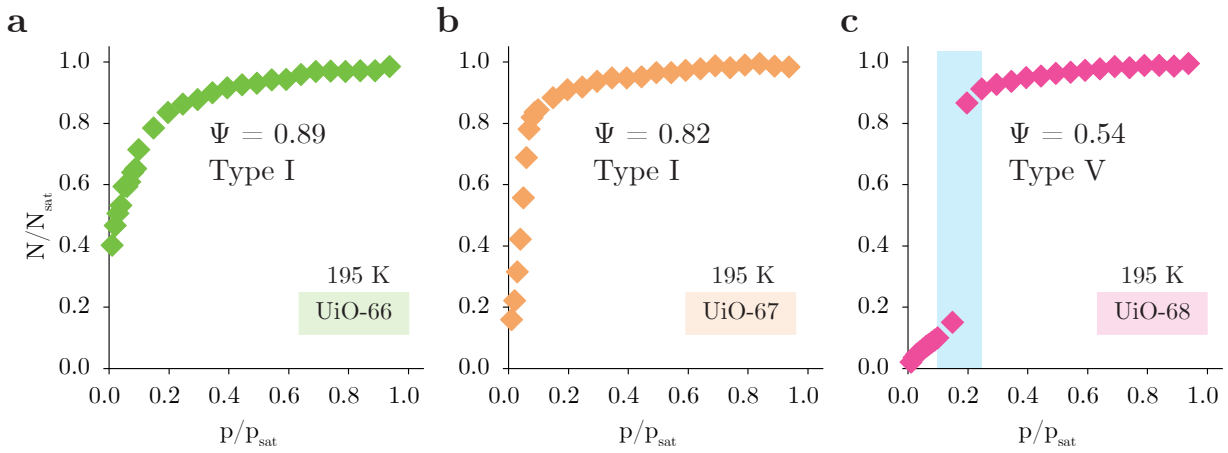

Figure S17: **CO_2 adsorption isotherms for the UiO-family at 195 K**
a UiO-66: Type I adsorption isotherm, **b** UiO-67: Type I adsorption isotherm, **c** UiO-68: Type V adsorption isotherm

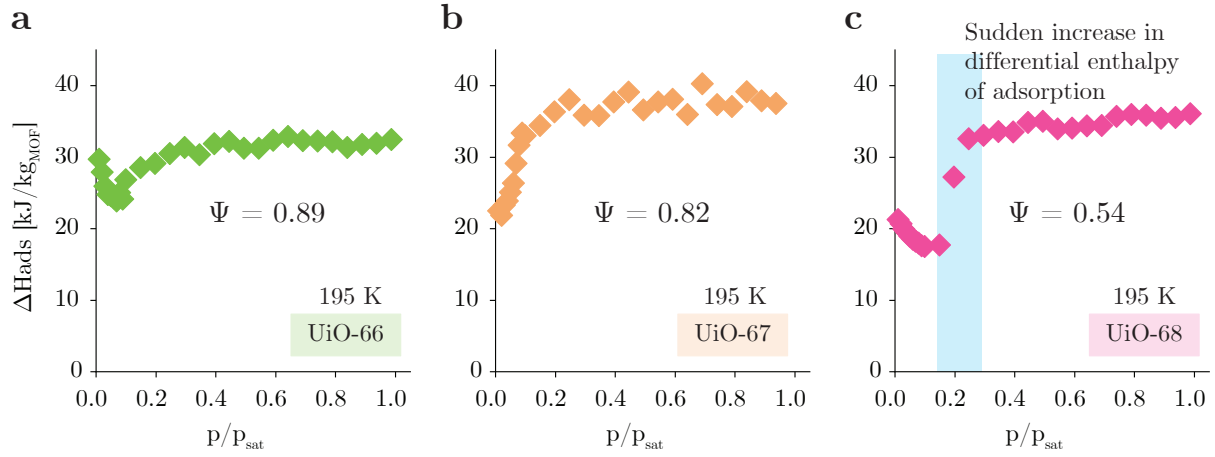

Figure S18: **Differential enthalpy of adsorption as a function of relative pressure**
a UiO-66, **b** UiO-67, **c** UiO-68

the pore size is increased. UiO-66 with a 6 Å pore has a type I adsorption isotherm (Fig. S17**a**), UiO-67 with a 9 Å pore has a type I adsorption isotherm (Fig. S17**b**), and finally

UiO-68 with a 15 Å pore has a Type V adsorption isotherm (Fig. S17**c**). This shows the capillary condensation of CO_2 does not take place in the case of UiO-66 and UiO-67 (the gradual increase in the number density of the adsorbate). Whereas in the case of UiO-68, an abrupt increase is seen (see the blue shaded region in Fig. S17**c**), which corresponds to capillary condensation.[6] Similar trends can be observed from the differential enthalpy of adsorption as a function of relative pressure (see Fig. S18). The energy budget for the UiO-

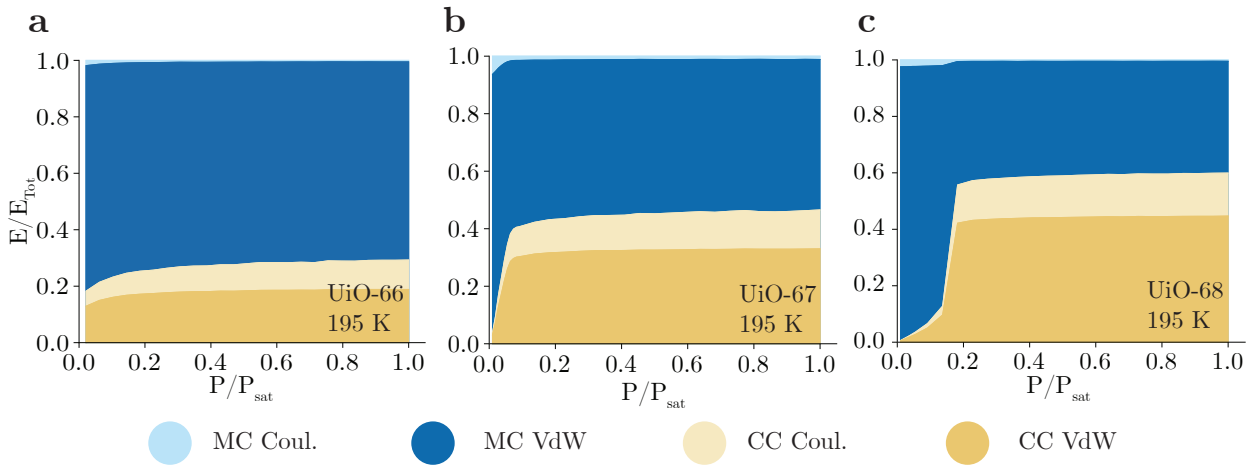

Figure S19: **Interaction energy budget for UiO-family**
a UiO-66, **b** UiO-67, **c** UiO-68

family is shown in Fig. S19. In all three cases, the MC coulombic interaction is infinitesimal. The contributions of inter-molecular interactions increase with increasing pore diameter, suggesting a higher number of molecules are adsorbed. Additionally, the ratio of MC - CC interactions increases drastically in the UiO-68 case around $p/p_0 \approx 0.2$ suggesting phase change inside the pore (capillary condensation). Finally, in Fig. S20, radial distribution functions are shown at different relative pressures. Fig. S20**a**, S20**b**, and S20**c** show the distribution of CO_2 around the central metal atom (Zr) in each case. For UiO-66, the center of the pore is the primary adsorption site as discussed in the main manuscript. Whereas in the case of UiO-67 and UiO-68 the primary adsorption site is near the metal atom at low pressure and shifts towards the center of the pore as the pressure increases. Fig. S20**d**, S20**e**, and S20**f** show the radial distribution function of the adsorbed CO_2 around adsorbed

CO_2. It is interesting to note that in all three cases, the RDF shows a "solid-like" structure. This might correspond to "capillary freezing" as the bulk CO_2 shows sublimation properties at 195 K. However, further investigation to understand the phase of adsorbed CO_2 inside UiO-family pores is needed.

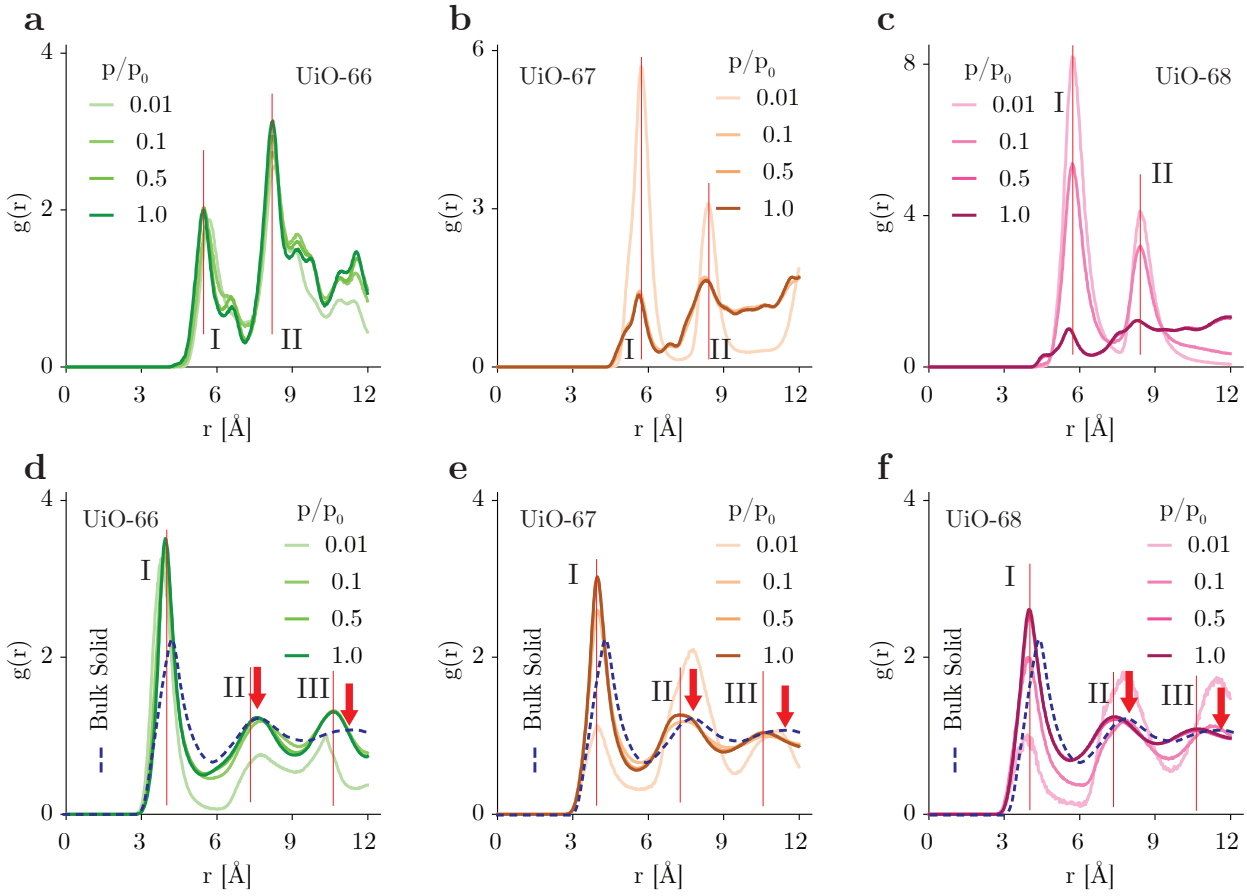

Figure S20: **Radial distribution functions**
RDF of adsorbed CO_2 around the central metal atom Zr in **a** UiO-66, **b** UiO-67, and **c** UiO-68
RDF of CO_2-CO_2 adsorbed in **d** UiO-66, **e** UiO-67, and **f** UiO-68

S5 Additional MOFs

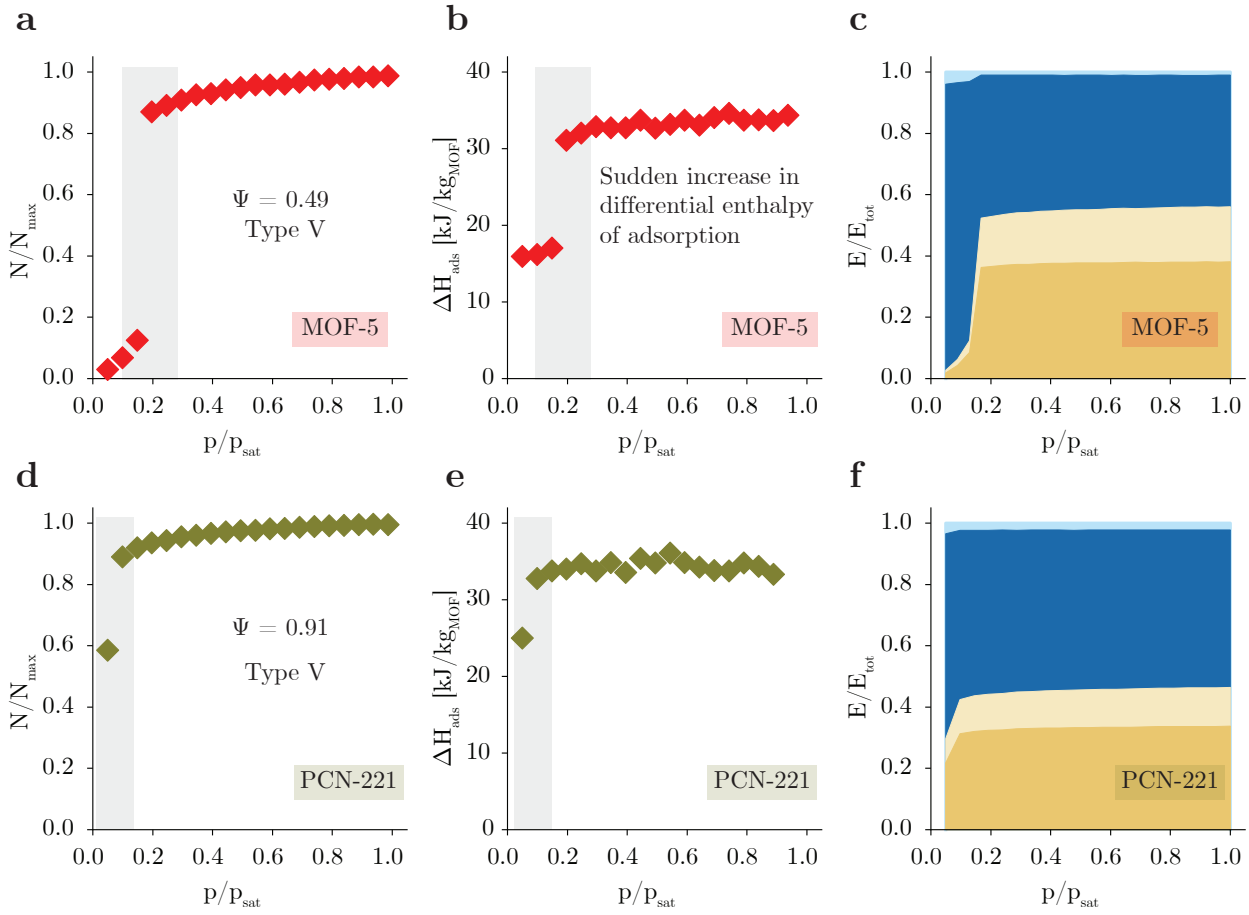

Figure S21: **Additional MOFs studied**
MOF-5: **a** Adsorption isotherm, **b** Differential enthalpy of adsorption, **c** Interaction energy budget
PCN-221: **a** Adsorption isotherm, **b** Differential enthalpy of adsorption, **c** Interaction energy budget

To understand the effect of pore structure on the adsorption characteristics we investigated CO_2 adsorption in MOF-5 which has all the other parameters (central metal atom, pore-size) similar to MOF-177. However, the structures of pores in each case are different. The results obtained are shown in Fig. S21**a**, Fig. S21**b**, and Fig. S21**c**. It can be observed that, despite different pore structures, different central metal atoms, and charge distribution the adsorption isotherms of MOF-177 (see Fig. **??c**), UiO-68 (see Fig. S17**c**), and MOF-5 (see Fig. S21**a**) are similar to each other, as the confinement parameter for each

all three MOFs lie within 0.4 and 0.6 (see Fig. **??b**). This shows the consistency of the one-dimensional model. However, in the case of PCN-221 where there are two metal sites (Cu and Zr), the adsorption isotherm is still type V despite the confinement parameter being greater than Ψ_{crit} ($\Psi = 0.91$) (see Figs. S21**d**, **e**, and **f**)

References

(1) Rappé, A. K.; Casewit, C. J.; Colwell, K.; Goddard III, W. A.; Skiff, W. M. UFF, a full periodic table force field for molecular mechanics and molecular dynamics simulations. *Journal of the American chemical society* **1992**, *114*, 10024–10035.

(2) Potoff, J. J.; Siepmann, J. I. Vapor–liquid equilibria of mixtures containing alkanes, carbon dioxide, and nitrogen. *AIChE journal* **2001**, *47*, 1676–1682.

(3) Klotz, I. M.; Walker, F. M.; Pivan, R. B. The binding of organic ions by proteins1. *Journal of the American Chemical Society* **1946**, *68*, 1486–1490.

(4) Buttersack, C. Modeling of type IV and V sigmoidal adsorption isotherms. *Physical Chemistry Chemical Physics* **2019**, *21*, 5614–5626.

(5) Mahle, J. J. An adsorption equilibrium model for Type 5 isotherms. *Carbon* **2002**, *40*, 2753–2759.

(6) Zsigmondy, R. Über die Struktur des Gels der Kieselsäure. Theorie der Entwässerung. *Zeitschrift für anorganische Chemie* **1911**, *71*, 356–377.